JOURNAL OF GUIDANCE, CONTROL, AND DYNAMICS
Vol. 19, No. 6, November–December 1996

Multivariable High-Authority Control of Plate-Like Active Structures

Kenneth B. Lazarus,* Edward F. Crawley,† and Charrissa Y. Lin‡
Massachusetts Institute of Technology, Cambridge, Massachusetts 02139

A dynamic modeling capability for plate-like structures with integrated strain actuators is developed using the Rayleigh–Ritz assumed-mode method. The analytical model is utilized to design multi-input, multi-output (MIMO) controllers for active plate-like test articles. High control authority linear quadratic Gaussian (LQG) and optimal projection compensators are designed using a control-law development procedure that combines performance objectives, physical measurements, and LQG design variables in a consistent manner. The control laws are implemented using a real-time digital-control computer. In addition, a stability robustness guideline is developed to predict, a priori, the amount of control authority that can be applied to the test articles without destabilizing high-frequency modes. Closed-loop benchtop experiments are performed to verify the open-loop analytical model, the stability robustness predictions, and the control-law development procedure; the experiments demonstrate the ability of integrated strain actuators to effect high-authority MIMO control on flexible plate-like structures. The results show that considerable disturbance attenuation can be achieved both in the quasi-steady response and over large bandwidths spanning many flexible modes.

Introduction

FUTURE space vehicle and aircraft performance criteria demand lightweight flexible structures such as solar arrays, antennas, mirrors, and lifting surfaces. Structural integrity and mission requirements call for low vibration and load levels. Because of these conflicting specifications for light weight and high dynamic performance, there exists a need for high-authority, large-bandwidth control systems. This can be achieved by designing multi-input, multi-output (MIMO) control laws for active composite structures with surface-mounted or embedded strain actuators. Distributed strain actuators, such as piezoceramics, provide a natural and logical mechanism for effecting distributed multiple actuator control and for implementing modern model-based control methodologies.

Active structures with integrated actuators have advantages over inertial (proof-mass) or articulated (aileron) actuators in that they offer direct control of the strain in the structure. One application of such a controlled plate-like structure is an active lifting surface that can be utilized for maneuver enhancement (command following), flutter and vibration suppression (plant regulation), and gust and load alleviation (disturbance rejection). Active lifting surfaces with distributed strain actuators have advantages over conventional aileron-controlled wings, which are subject to loss of effectiveness at high dynamic pressures and limited servomotor bandwidths.

The objective of this paper is to show the ability of strain-actuated plate-like active structures to effect high-authority, large-bandwidth control in a benchtop configuration. For this purpose, the dynamic characteristics of complex strain-actuated composite plate test articles are first modeled analytically and then verified experimentally. Next, the analytical model is used to derive high-authority, large-bandwidth MIMO compensators based on a quadratic cost function and linear quadratic Gaussian (LQG) optimal control theory. The control schemes then are assessed analytically to determine their effectiveness based on the closed-loop quadratic cost index and verified experimentally by bench-top closed-loop testing. Closed-loop state vs control-cost results are reported to demonstrate the significant disturbance attenuation obtainable by applying modern control techniques to active plate-like structures. Reporting the closed-loop results in this manner not only shows the performance achieved, but also displays the control authority used in relation to the maximum possible and aids in determining the cause of performance limitations. In addition, practical tools needed for predicting, a priori, closed-loop performance limits from open-loop experiments and analytical models (i.e., stability robustness) are developed and correlated with the actual limits found during closed-loop testing. This work forms the precursor for the active aeroelastic-control wind-tunnel experiments that will be reported in a future paper.

Received Jan. 20, 1995; revision received April 24, 1996; accepted for publication June 17, 1996.

*Graduate Research Assistant, Space Engineering Research Center. Member AIAA.

†Professor of Aeronautics and Astronautics, Space Engineering Research Center. Fellow AIAA.

‡Graduate Research Assistant, Space Engineering Research Center. Student Member AIAA.

Experimental Setup

The test articles were constructed at the Massachusetts Institute of Technology Space Engineering Research Center and are described in detail elsewhere.[1] Figure 1 shows a diagram of the strain-actuated active-lifting-surface test articles. A 6061 aluminum benchmark article was designed and tested as was a $[+30_2/0]_s$ bending/twist coupled AS4/3501-6 graphite/epoxy (G/E) plate. The test articles had a thickness-to-chord ratio of approximately 1%, and were clamped at the root.

The Piezoelectric Products, Inc., G-1195 piezoceramic actuators were intended not only to provide actuation but also to make up a substantial portion of the structure itself. Each of the active test

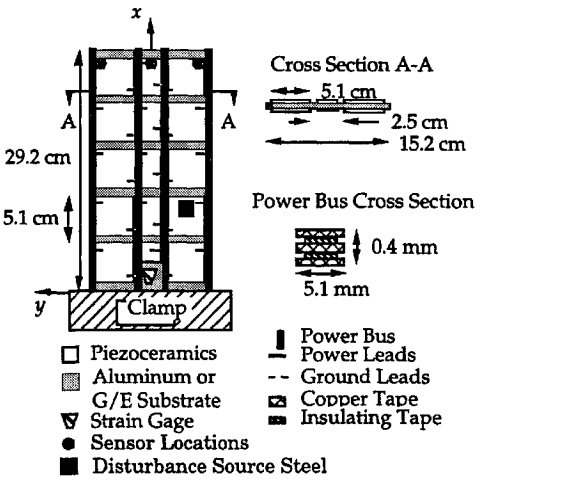

Fig. 1 Model strain-actuated active lifting-surface test article.

articles had approximately 70% of each surface covered with the surface-bonded piezoceramic strain actuators. The 10-mil (0.254-mm) strain actuators accounted for 31.3 and 52.0% of the aluminum lifting-surface volume and weight and 30.1 and 62.3% of the G/E lifting-surface volume and weight, respectively. These piezoceramic actuators increased spanwise bending stiffness of the aluminum and G/E plates by 201 and 437%, respectively, over the nominal substructure stiffness. Strength measurements were not obtained, however; because of their brittle nature, the piezoceramics are not expected to add strength. Under severe flutter loading and deflections, the piezoceramic actuators of this test article and others[2] did not debond. Some cracks were observed, but these did not reduce the piezoceramic actuation effectiveness.[2]

In addition to the test articles, many other components are required to perform control experiments. These components, which include hardware such as sensors, a digital control processor, power amplifiers, and a disturbance source, are fully described elsewhere.[3] The motion of the test articles was measured by three noncontacting Keyence LB-70 laser displacement sensors. It is acknowledged that actual lifting surfaces are not able to take advantage of such displacement measurements. However, actual lifting surfaces do have ample space (not available on the small-scale model lifting surfaces) for accelerometers, the output of which can be integrated to yield measurements equivalent to the displacement measurements made in this study.

A noncontacting magnetic proximity probe was driven as an actuator to provide a disturbance source in the benchtop configuration. The magnetic field created by the proximity probe produced a disturbance force on a 1-in.-square steel target attached to each test specimen. This disturbance force was applied at the quarter chord to simulate forces similar to those that will be encountered during wind-tunnel testing. The steel target was placed at approximately the quarter span because at this location the disturbance source was found to excite the test articles most effectively.

Analytical Modeling

Lifting-Surface Structural Model

A detailed model is essential for implementing high-authority, large-bandwidth control systems. Accurate knowledge of the system poles and zeros is required to develop effective control schemes. To achieve such a high-fidelity model, both the active test articles (the plant) and the additional mass and stiffness of the signal and power conditioning circuitry are modeled analytically. An identification model could be used for control, but these models tend not to be physically based and do not provide as much insight into the physical problem as an analytical model. In addition, the current test article is a basic structure that lends itself well to analytical modeling.

The active test articles with surface-mounted strain actuators are modeled as integrated components of a composite structure. By modeling the substructure, piezoceramic actuators, and epoxy layers as plies of a laminated plate, the appropriate strain-energy relations can be derived using Kirchoff plate assumptions.[1,4,5]

The Rayleigh–Ritz assumed-mode method is used to formulate the lifting-surface equations of motion from the strain-energy relations.[6] It has been observed through structural modeling experience that Ritz models are better suited than finite element models for correctly identifying not only the natural frequencies[7] but also the system transmission zeros and individual actuator/sensor transfer-function zeros. However, obtaining accurate results requires that a well-chosen set of assumed modes be used, and for a more complicated test article, a finite element model would be required.

Twenty assumed modes are utilized. The 20 modes include 5 spanwise beam bending (B), 4 spanwise torsional (T), 2 chordwise bending (C), and 4 extensional (E), as well as 2 static and 3 segmented modes. The spanwise bending modes, which have assumed constant chordwise distribution, are found from the exact solution of a cantilever-free beam.[8] The spanwise torsional modes are calculated by performing a torsion partial Ritz analysis (assumed linear chordwise distribution), to include root warping stiffness effects.[9] The chordwise bending modes are the exact solution of a free–free beam with a quadratic spanwise distribution.

In addition to the usual dynamic mode shapes, modes are assumed that are not associated with the solution of any eigenvalue problem. A quadratic spanwise static and a quadratic chordwise static assumed mode are included to model the strain energy associated with a constant distributed bending moment. Also, two segmented spanwise modes and one segmented chordwise mode are assumed to correctly model the strain energy stored in the aluminum or G/E test-article substructure at the relatively soft locations in the gaps between the piezoceramics. Segmented assumed modes have nonzero curvature in areas that do not contain piezoceramics and zero curvature in areas that do. The spanwise x distributions of the chordwise static and segmented modes are calculated from a chamber partial Ritz analysis (assumed quadratic chordwise distribution) similar to that used to calculate the spanwise distribution of the torsional modes. Inclusion of the static and segmented modes, as well as performing the partial Ritz analysis, is essential for correctly predicting the system poles, transmission zeros, and steady-state transfer-function magnitudes. Finally, two spanwise and two chordwise in-plane modes are also included to allow for extensional actuation.

Note that the assumed mode shapes (i.e., 1–11, 13, 16, 17, and 19), which are dependent on plate structural stiffnesses, are calculated using uniform averaged properties. The stiffness properties are averaged by weighting the stiffness of each section of the plate (substructure with piezoceramic, nongrooved substructure, and grooved substructure) by the area of the section relative to the total plate area. Further Ritz analysis details can be found elsewhere.[3]

The Rayleigh–Ritz analysis method combines the plate strain-energy relations and the assumed modes to calculate the plate equations of motion. This analysis yields the modal mass $\boldsymbol{M}$, stiffness $\boldsymbol{K}$, and piezoelectric $\boldsymbol{F}_\Lambda$ and disturbance $\boldsymbol{F}_d$ forcing matrices[10]

$$\boldsymbol{M}\ddot{\boldsymbol{q}} + \boldsymbol{K}\boldsymbol{q} = \boldsymbol{F}_L + \boldsymbol{F}_d \tag{1}$$

The generalized displacements $\boldsymbol{q}$ in Eq. (1) are related to the in- and out-of-plane displacements through the assumed-mode shapes ψ_i, which are functions of both the spanwise x and the chordwise y coordinates.

The experimentally measured and analytically predicted pole frequencies of the test articles are listed in Table 1. The Ritz predictions were within 5 and 9% of the experimentally measured values in the control bandwidth (200 Hz) for the aluminum and G/E plates, respectively. Note that the analysis method had the greatest difficulty in predicting the aluminum test article chordwise bending natural frequency (1C), due to sensitivity of this plate to the change in stiffness caused by the power bus grooves. In contrast, observe the nominal chordwise bending frequency error for the G/E plate whose stiffness sensitivity was much lower.

In addition to the relatively small error in the predicted and measured natural frequencies, the Ritz analysis also was able to accurately compute the modal residues such that the static response was correctly predicted and the I/O transfer function omitted no zeros and correctly ordered the poles and zeros. For example, the predicted frequencies of the first two zeros of the transfer function of the disturbance to the leading-edge sensor (y_1/d) (see Fig. 3) were predicted within 7 and 5% of the experimental values, respectively. This accuracy was typical of the results obtained and sufficient for designing high-authority control laws.

Table 1 Experimentally measured and analytically predicted test-article natural vibration frequencies and dominant mode shapes

	Al Plate			G/E Plate		
Mode	Exp., Hz	Ritz, Hz	% Error	Exp., Hz	Ritz, Hz	% Error
1B	7.44	7.79	4.7	6.88	7.44	8.1
1T	36.6	36.0	−1.6	35.3	35.3	0.0
2B	49.5	50.4	1.8	47.8	49.0	2.5
2T	117	122	4.3	114	124	8.8
3B/1C	143	149	4.2	138	145	5.1
1C/3B	204	185	−9.3	166	161	−3.0
3T	223	235	5.4	215	242	12.6
4B	283	298	5.3	282	306	8.5
4T	370	390	5.4	353	405	14.7

In general, the Ritz model predicted the poles of the lifting surface with the aluminum substructure with greater accuracy than the G/E substructure because of difficulties in obtaining accurate estimates of the stiffness properties of thin laminated G/E structures. The anisotropic stiffness properties of the G/E substructure caused both the natural vibration mode shapes and dominant mode order to differ from that of the aluminum plate.

The model was refined further by updating the damping ratio ζ_i and natural frequencies ω_i using experimental frequency response data. Incorporation of the experimental data into the analytical model was facilitated by mapping the system of Eq. (1) to modal coordinates, using the eigenvectors of the Ritz model. The measured damping ζ (estimated on the basis of the half-power bandwidth technique) was added to the modal system, and the stiffness matrix was updated using the experimentally measured frequencies and the original eigenvectors.

Including the experimentally determined damping estimates in the model proved extremely important for compensator design because this quantity directly affects the dynamic amplification of each mode, and therefore the plant/compensator loop gain and degree of notching required by the compensator in the rolloff region. In contrast, it was found that controllers designed from models with the experimentally updated stiffness matrices achieved no better performance than those designed from the analytically predicted Ritz stiffness.

Full-Order Analytical Model

The plant model of any controlled system must be augmented to include the dynamics of sensors, actuators, and any other electronic components in the feedback path such as antialiasing filters and amplifiers. A block diagram of the system components to be modeled is shown in Fig. 2. The full plant system had 73 states; 40 of the states were associated with the 20 structural modes. The remaining states resulted from the dynamics of three optical sensors (each modeled with 1 pole at 700 Hz) and antialiasing filters (modeled with 2 poles at 1000 Hz for each of the 3 sensor outputs, and 2 poles at 2500 Hz for each of the 12 control inputs). This large-order evaluation model was used to calculate the open- and closed-loop disturbance transfer functions and to evaluate the stability and performance of the control laws designed. The dynamics of this large-order open-loop system can be described in either the state-space representation

$$\dot{x} = Ax + Bu + Ld \qquad y = Cx \tag{2}$$

or the transfer function representation

$$\begin{aligned} y &= CG_c(s)u \qquad & G_c &= C(sI - A)^{-1}B \\ y &= CG_d(s)d \qquad & G_d &= C(sI - A)^{-1}L \end{aligned} \tag{3}$$

Model Order Reduction

The 73-state evaluation model was reduced to a lower-order design model using balanced model truncation.[11] The states associated with the Hankel singular values greater than 0.1% of the maximum singular value are retained in the model. The steady-state components of the discarded states also are retained in the model.

This procedure reduced the 73-state evaluation model to a 22-state design model. It was found that the disturbance-to-sensor output (y/d) and control-input-to-sensor-output (y/u) transfer functions of the design model were nearly identical to those of the evaluation model in the evaluation bandwidth (500 Hz). Further, it was found that increasing the order of the design model had no effect on the designed controllers or their performance.

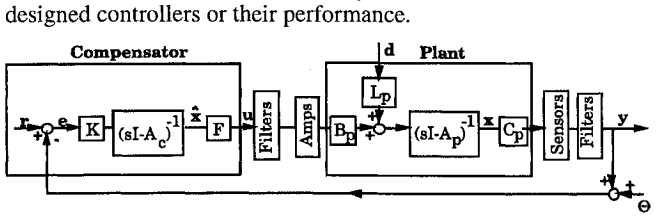

Fig. 2 Block diagram of the experimental system including the lifting surface (A_p, B_p, C_p, and L_p), compensator (A_c, K, and F), disturbance (d), and measurement noise (Θ).

Control-Law Synthesis

The first step necessary in designing control laws for particular systems is to define the performance objectives and metrics for the controlled systems. The dynamic aeroelastic-control performance objectives of greatest interest include flutter suppression, vibration suppression, and gust alleviation. In terms of control system design, these issues translate into those of stability, plant regulation, and disturbance rejection, respectively. Because a well-regulated plant automatically carries the properties of guaranteed stability and good disturbance rejection, the control problem reduces to first designing control laws so that the plant is well regulated.

LQG Compensator Design

The LQG compensator contains dual halves: a linear quadratic regulator (LQR) full-state feedback compensator and a Kalman filter estimator. The state cost for the LQR compensator was chosen as the sum of the output y rms response squared. Similarly, the control cost was chosen to be the sum of the control u rms response squared. The total cost J was therefore

$$\begin{aligned} J &= \int_0^\infty [\bar{y}^T\bar{y} + \rho\bar{u}^T\bar{u}]\,dt = \int_0^\infty [x^TQx + \rho u^TRu]\,dt \\ Q &= [C/y_{\max}]^T[C/y_{\max}] \qquad R = I/u_{\max}^2 \end{aligned} \tag{4}$$

where ρ is the relative state to control weighting design parameter. The scaled outputs $\bar{y}$ and inputs $\bar{u}$ were calculated by normalizing the physical outputs and inputs by their maximum values. The maximum outputs $y_{\max}$ were estimated on the basis of maximum expected sensor outputs caused by the disturbance source (6.35 V). The maximum control inputs $u_{\max}$ were taken to be those that could be generated by the control computer (± 10 V), because the amplifier gains (fixed at 20 to generate a maximum of ± 200 V) were already included in the system model.

The Kalman-filter half of the problem was set up by defining disturbance and sensor noise covariance matrices based on laboratory measurements of the disturbance source intensity and the accuracy of the laser displacement sensors. Such measurements are useful starting points for determining the intensities of the disturbance and measurement noise covariance matrices. However, in reality the intensities of these stochastic processes, which do not actually have zero means or white frequency distributions, are not known. Thus, these intensity matrices are used as design tools in a manner similar to the control weighting ρ. In this study, the disturbance intensity was normalized by its maximum value and fixed at unity because the disturbance signal used in the experiments was always the maximum value.

The measurement noise intensity was computed on the basis of sensor accuracy and the maximum expected sensor outputs. This normalized value was found to be 0.3%. However, to provide stability robustness to unmodeled and mismodeled plant dynamics, the intensity of the measurement noise was assumed to be an order of magnitude greater and was assumed to vary from this nominal value. Thus, the measurement noise was used as a free parameter in the Kalman filter design.

In state-space form, the compensator dynamics are

$$\dot{\hat{x}} = A_c\hat{x} + Ke \qquad u = F\hat{x} \tag{5}$$

where the error signal e is equal to the command r minus the sum of the output y and the measurement noise Θ. The model-based compensator dynamics are described by

$$A_c = A - BF - KC + KDF \tag{6}$$

The reader is referred to Lazarus[3] for compensator design details, including numerical values of the intensity matrices and the resulting compensator gains, poles, and transmission zeros.

Because of a tradeoff between the number of control outputs and the speed at which these outputs could be generated, three actuation groups were created from the piezoceramic wafers. The three groups were formed by first pairing each of the piezoceramics on opposite sides of the neutral axis, thus creating individual bending actuator pairs. One actuator group was then formed from the five actuator

pairs nearest the leading edge of the lifting surface (u_1), the second group of the five actuator pairs centered at the midchord (u_2), and the third group of the five actuator pairs near the trailing edge (u_3). These actuators were used in all control designs. All three of the laser displacement sensors were utilized in all of the experiments performed.

Controller Order Reduction

To facilitate implementation on the real-time control computer, the 22nd-order LQG compensators were reduced to 14th-order compensators, using the ordered Hankel singular value procedure described previously. As an alternative design procedure, reduced 14-state compensators were computed directly from the design model using a fixed-architecture optimal projection gradient search technique.[12] Optimal projection designs differ from the two-step (design and reduce) process in that the compensators are designed with the model order incorporated in the equations. The optimal projection compensators were compared to the reduced-order LQG compensators for the purpose of assessing the effect of ad hoc reduction of compensators.

The equations describing the reduced-order LQG or optimally projected compensators could be expressed in the state-space form

$$\dot{\hat{x}} = A_{cc}\hat{x} + K_c e \qquad u = F_c\hat{x} + D_c e \tag{7}$$

or the transfer-function form

$$u = K(S)e \qquad K(s) = F_c(sI - A_{cc})^{-1}K_c + D_c \tag{8}$$

where A_{cc} contains the reduced-order compensator dynamics and D_c is a compensator feed-through term that results from the reduction process. Note that the additional subscript c differentiates the reduced-order compensators [Eqs. (7) and (8)] from the original designs [Eqs. (5) and (6)].

Analytical and Experimental Results

The ability of the procedure described to derive effective controllers for the active test articles was determined through closed-loop benchtop testing and numerical simulation. The compensators were evaluated analytically for stability and performance, using the 73-state evaluation model. Performance was evaluated by comparing the experimentally measured and analytically predicted closed-loop disturbance attenuation to the open-loop output $G_d(s)$ described by Eq. (3). The closed-loop dynamic response was calculated using the state-space representation

$$\begin{bmatrix}\dot{x}\\ \dot{\hat{x}}\end{bmatrix} = \begin{bmatrix}A - BD_cC & -BF_c\\ K_cC & A_{cc}\end{bmatrix}\begin{bmatrix}x\\ \hat{x}\end{bmatrix} + \begin{bmatrix}L\\ \emptyset\end{bmatrix}d$$
$$y = [C \quad \emptyset]\begin{bmatrix}x\\ \hat{x}\end{bmatrix} \tag{9}$$

Performance also was assessed by comparing the experimentally measured and analytically predicted state cost vs control cost of each controller. The closed-loop state cost is directly related to the rms response of the outputs, and measures the performance of each control design. Similarly, the control cost is directly related to the rms response of the control inputs and is a measure of the amount of control used. By solving the Lyapunov equation associated with the closed-loop system,

$$\begin{bmatrix}\dot{x}\\ \dot{\hat{x}}\end{bmatrix} = \begin{bmatrix}A - BD_cC & -BF_c\\ K_cC & A_{cc}\end{bmatrix}\begin{bmatrix}x\\ \hat{x}\end{bmatrix} + \begin{bmatrix}L & -BD_c\\ \emptyset & K_c\end{bmatrix}\begin{bmatrix}d\\ Q\end{bmatrix} \tag{10}$$

the state and control costs can be found directly from the covariance matrices

$$\text{State cost} = \text{Trace}(QE[xx^T])$$
$$\text{Control cost} = (1/\rho)\,\text{Trace}(GR^{-1}G^T E[\hat{x}\hat{x}^T]) \tag{11}$$

Performance Results

The frequency response of the open- vs closed-loop analytical and experimental disturbance to leading-edge sensor (y_1/d) transfer functions are displayed in Figs. 3 and 4 for the aluminum and G/E test articles, respectively. Notice the good agreement between the analytical model and the experimental results. The agreement between the model and the experiment indicates that the dynamics of the other system components (such as sensor rolloff and filter dynamics) were modeled correctly. Further, the excellent closed-loop performance validates the compensator design, order reduction, and digital implementation methods utilized.

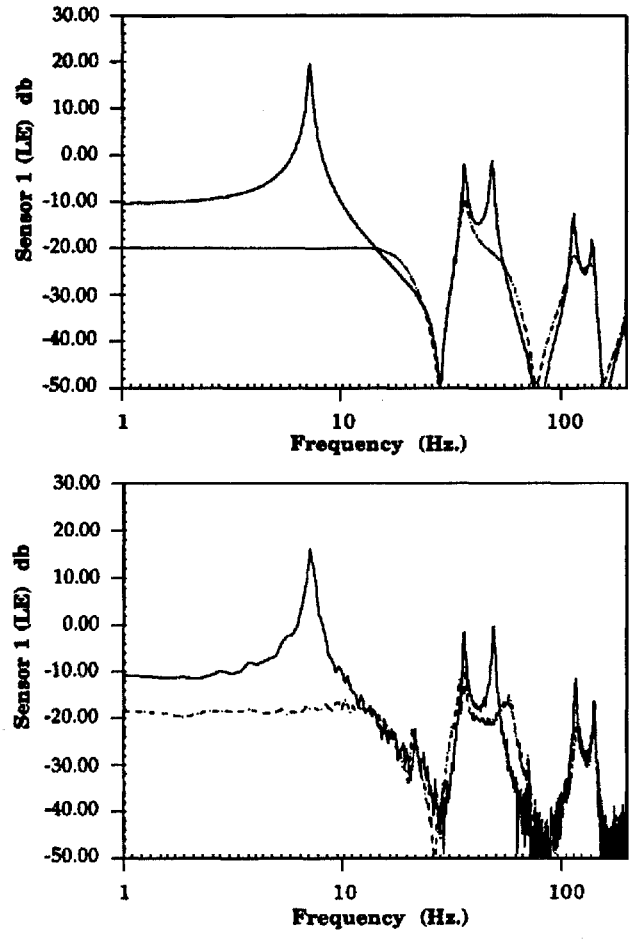

Fig. 3 Analytical and experimental open- and closed-loop frequency response of the aluminum test article for a LQG compensator designed with $\rho = 10^{-2}$ and the sensor noise estimated at 3%.

Figures 3 and 4, which display the tip displacement attributable to a broadband (500 Hz) excitation from the magnetic probe, illustrate the high-authority, large-bandwidth nature of these controller designs. Significant amounts of damping were introduced into the first four structural modes by these control designs ($\rho = 10^{-2}$) without destabilizing any high-frequency modes. For both test articles, the magnitude of the closed-loop frequency response was reduced from that of the open-loop system (which had an estimated 1.5% structural damping in each mode) by approximately 30, 10, 20, and 10 dB in the first four modes, respectively. Comparison of Figs. 3 and 4 shows the increased torsional (second and fourth modes) control authority of the bending/twist coupled G/E plate; however, this additional torsional control was not as pronounced as expected in the benchtop tests. In addition to reducing the steady-state response by approximately 10 dB, note that the controller has succeeded in completely eliminating the resonant behavior of the first structural mode in both test articles. These results demonstrate that strain actuation, which provides direct control of the strain in the structure, can be used to implement high-authority control designs.

Stability Robustness

Transfer functions, such as those in Figs. 3 and 4, show the ability of strain actuation to effect significant amounts of disturbance attenuation, but offer no information with regard to the amount of control authority used or the amount that can be applied to the

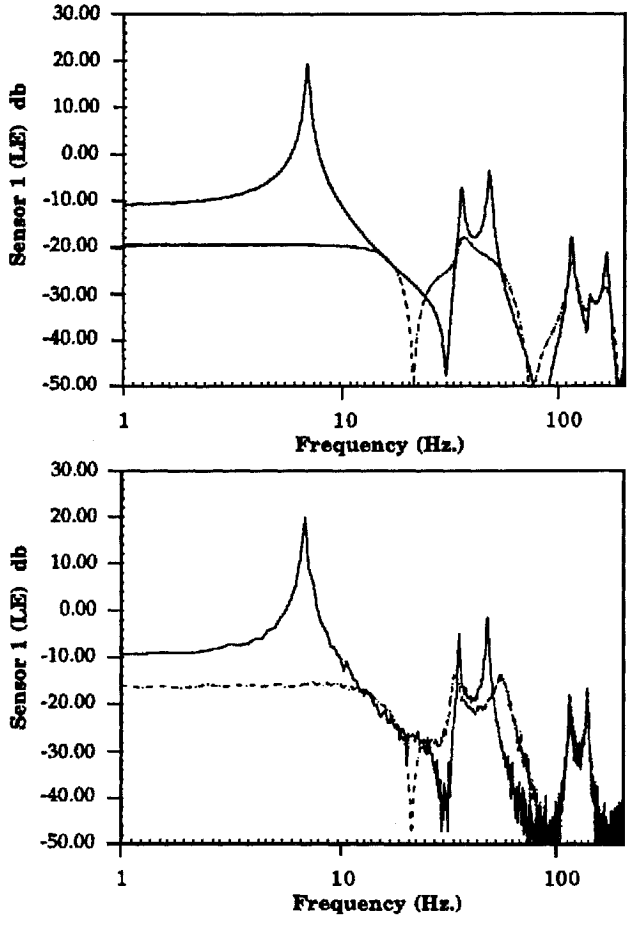

Fig. 4 Analytical and experimental open- and closed-loop frequency response of the G/E test article for a LQG compensator designed with $\rho = 10^{-2}$ and the sensor noise estimated at 3%.

system before errors in the analytical model cause instabilities. For this purpose, a stability robustness test is needed that can predict the control authority that can be applied successfully to the system. Unfortunately, most currently employed stability robustness tests are overly conservative. One stability robustness test requires the maximum singular value of the closed-loop control transfer function $\sigma_{\max}[C(s)]$ to be less than the reciprocal of the maximum singular value of the multiplicative model error $1/\sigma_{\max}[\Delta(s)]$ acting at the plant output[13]:

$$\sigma_{\max}[C(s)] < \frac{1}{\sigma_{\max}[D(s)]}$$

$$C(s) = [I + T(s)]^{-1}T(s) \tag{12}$$

$$D(s) = [G_c(s)_{\exp} - G_c(s)]G_c(s)^{-1}$$

where

$$T(s) = G_c(s)K(s)$$

where $T(s)$ is the loop transfer function (with the loop broken at the sensor outputs). The actual model error is computed using the evaluation-model-calculated $G_c(s)$ and the experimentally measured $G_c(s)_{\exp}$ control transfer function [Eq. (3)] matrices. This robustness test guarantees stability.

Unfortunately, this method yields overly large error maximum singular values and an extremely conservative stability robustness test. The conservatism of this nominal test is illustrated in Fig. 5, which shows the maximum singular values of the closed-loop control transfer function $\sigma_{\max}[C(s)]$ and the inverse error matrix $1/\sigma_{\max}[\Delta(s)]$ for the aluminum test article. Note that the test is violated (predicting instabilities) over the entire evaluation bandwidth for a compensator designed with a control weighting $\rho = 1$,

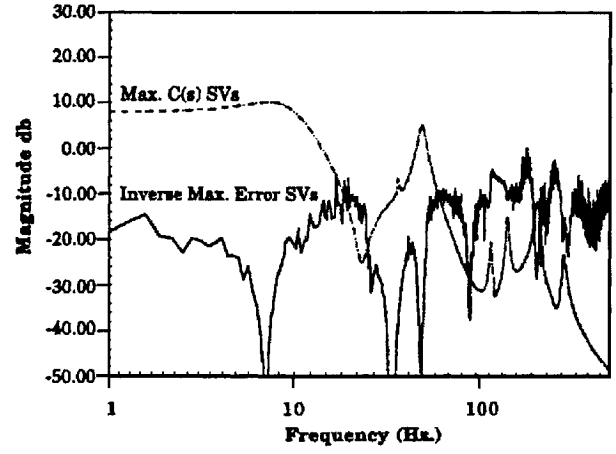

Fig. 5 Closed-loop $C(s)$ maximum singular values and the reciprocal of the error $\Delta(s)$ maximum singular value for the aluminum plate with a LQG compensator designed with $\rho = 1$ and the sensor noise estimated at 3%. The plot shows the inability of the nominal robustness test to predict stability.

two orders of magnitude greater (i.e., producing much lower control gain) than that of the stable high-performance compensator depicted in Fig. 3. Obviously, this nominal test is very conservative and not a useful tool for predicting the amount of control effort that can be utilized before instabilities are encountered.

Motivated by the deficiencies of this nominal method, a stability robustness guideline was derived to develop a more realistic estimate of the maximum control effort that can be utilized before such instabilities occur. This guideline is derived on the basis of the small-gain theorem, as is the test described above.[14] However, rather than break the loop transfer function at the sensor outputs [as in Eq. (10)], a singular value decomposition is performed on the plant control transfer function, $G_c(s) = U\Sigma V$, and a new loop transfer function T_Σ is found by breaking the loop at the output of the plant singular values Σ. A new closed-loop transfer function matrix C_Σ is then formed and compared to the error Δ_Σ, which is found from the calculated and experimentally measured singular values.

Because the error Δ_Σ is calculated from the singular values, the error matrix is made up of only diagonal terms, each of which is essentially a measure of the percent error in the particular singular value. This method disregards any difference between the analytical and experimental unitary matrices, $U(s)$ and $V(s)$, in the formulation of the multiplicative error. However, because the stability robustness guideline is derived from the small-gain theorem, which does not consider directional information, disregarding the directional information contained in the unitary matrices is considered consistent and leads to a modified stability robustness guideline useful for actual controlled flexible structures:

$$_{\max}[C_\Sigma(s)] < \frac{1}{\sigma_{\max}[D_\Sigma(s)]}$$

$$C_\Sigma(s) = [I + T_\Sigma(s)]^{-1}T_\Sigma(s) \tag{13}$$

$$D_\Sigma(s) = [S(s)_{\exp} - S(s)]S(s)^{-1}$$

where $G_c(s) = U(s)S(s)V(s)$ and $T_\Sigma(s) = V(s)K(s)U(s)S(s)$.

This stability robustness guideline carries no guarantee of stability (in contrast with the nominal conservative test) but was found to be accurate at predicting robustness to model errors. This guideline was applied to the strain-actuated flexible structures used in this study. Example results are plotted in Figs. 6 and 7 for the aluminum and G/E plates, respectively. In the region where control is being effected, the control law utilizes directional (phase) information to maintain stability even when the small-gain theorem is violated. However, in the rolloff region (above 120 Hz), the compensator uses gain notching to avoid destabilizing higher modes, as shown in Fig. 8, and makes no use of any directional information. It is in this rolloff region that any violation of the robustness guideline will cause an instability.

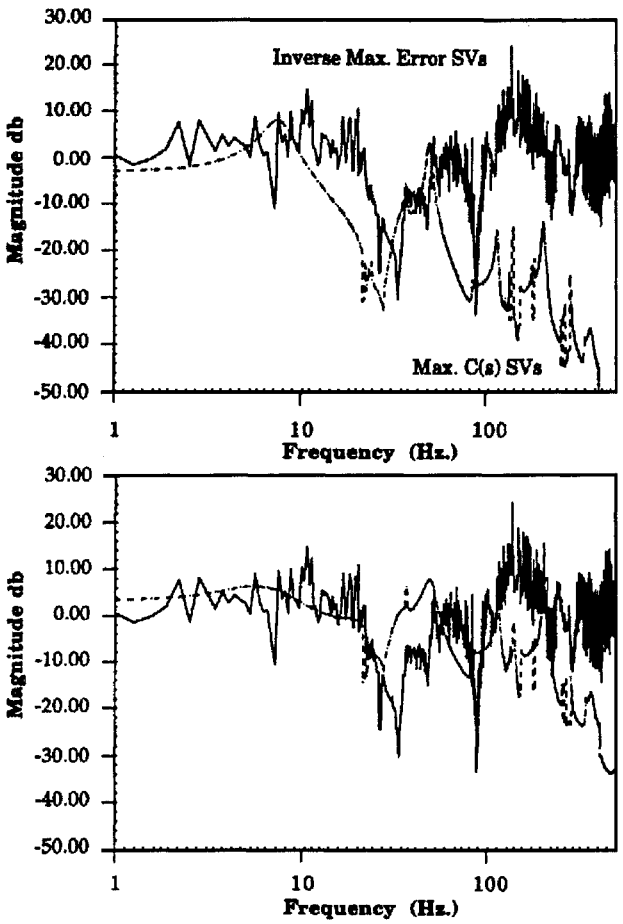

Fig. 6 Closed-loop control transfer function $C_\Sigma(s)$ maximum singular value and the reciprocal of the error $\Delta_\Sigma(s)$ maximum singular value for the aluminum plate with an LQG compensator designed with ρ = 10^0, and 10^{-2}, and the sensor noise estimated at 3%. The plot shows the ability of the modified robustness test to predict stability.

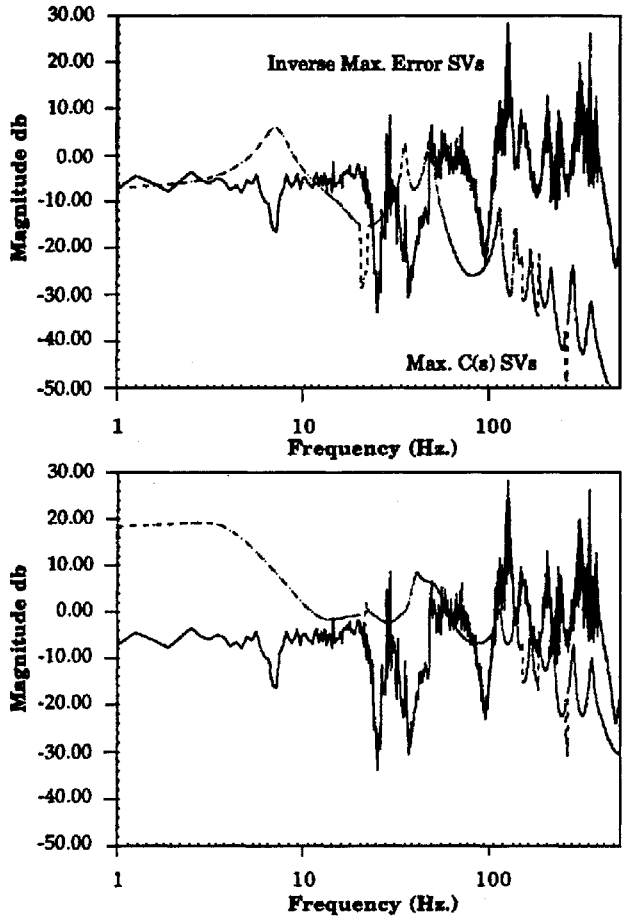

Fig. 7 Closed-loop control transfer function $C_\Sigma(s)$ maximum singular value and the reciprocal of the error $\Delta_\Sigma(s)$ maximum singular value for the G/E plate with an LQG compensator designed with $\rho = 10^0$ and 10^{-2}, and the sensor noise estimated at 3%. The plot shows the ability of the modified robustness test to predict stability.

Figures 6 and 7 clearly show that the new guideline predicts stability for the $\rho = 1$ compensator design {the maximum singular values of the closed-loop transfer function $\sigma_{\max}[\boldsymbol{C}(s)]$ do not penetrate through the inverse of the error maximum singular values $1/\sigma_{\max}[\Delta(s)]$ in the controller rolloff region}. In contrast, the conservative stability robustness test (Fig. 5) predicts that instabilities will occur {$\sigma_{\max}[\boldsymbol{C}(s)]$ penetrates and extends above $1/\sigma_{\max}[\Delta(s)]$ in the rolloff region}. Note that this compensator design was found experimentally to be stable.

As the relative control weighting is decreased and the control designs utilize higher gains, the maximum singular value of the closed-loop transfer function $\sigma_{\max}[\boldsymbol{C}(s)]$ increases and moves closer to the reciprocal of the maximum singular value of the error $1/\sigma_{\max}[\Delta(s)]$ in the rolloff region. The plots indicate that model errors, even if relatively small, will eventually cause instabilities as the gain increases. These instabilities can be attributed to notches found in the rolloff region of LQG compensators, which become sharper and deeper as the gain is increased, and eventually miss the targeted mode.

For a control weight of $\rho = 10^{-2}$, the two curves are very close in the rolloff region, indicating that the amount of control used is very close to causing an instability. It was found experimentally that controllers with relative control weights greater than or equal to 10^{-2} were stable, whereas those designed with control weights less than 10^{-2} were unstable for both test articles, demonstrating the usefulness of this stability robustness guideline.

Performance Robustness Correlation

The performance robustness can be gauged by plotting the analytically predicted and experimentally measured closed-loop state cost vs control cost normalized by the open-loop state cost. Cost curves

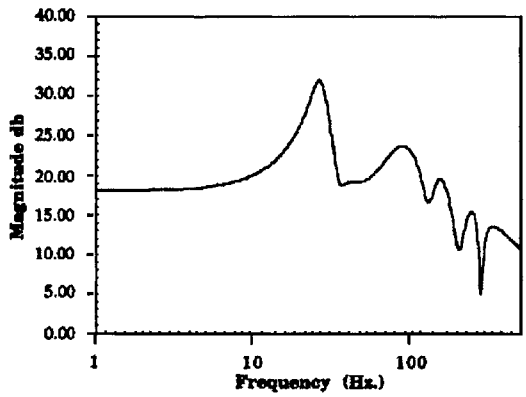

Fig. 8 Typical compensator maximum singular value plot. The graph shows the high gain of the control bandwidth and notching that occurs in the rolloff region.

for the compensators designed with an assumed measurement noise of 3% are plotted in Fig. 9 for the aluminum test article. Analytically predicted cost curves are shown in Fig. 9 for design-model LQG, reduced-order LQG, and optimal projection compensators. The figure shows that the reduced-order LQG compensators deviated from the design-model compensators only for those designs with very high control gains ($\rho = 10^{-3}$ and 10^{-4}). The reduced-order LQG and optimal-projection experimentally measured cost curves are compared to the analytical results in Fig. 9. Note that the two experimental compensator cost curves provide the same disturbance attenuation performance and that these results compare favorably to those predicted analytically.

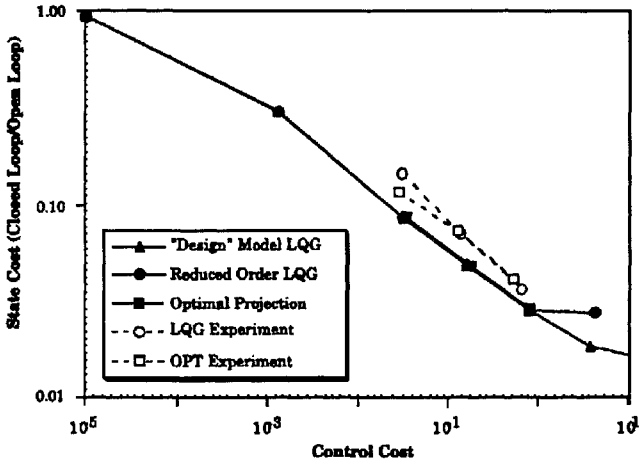

Fig. 9 Analytical and experimental state vs control closed-loop cost curves for the aluminum test-article compensators designed for a sensor noise estimate of 3%.

It was determined analytically that the high-gain stable reduced-order compensator (relative state-to-control cost weighting $\rho = 1e^{-3}$) decreased the state cost by 97.2% (83.4% rms) or 31.2 dB (15.6 dB rms) for the aluminum-plate test article. However, model errors prevented such performance from being achieved experimentally. As seen in Fig. 9, the best controller implemented ($\rho = 10^{-2}$) was analytically predicted to decrease the state cost by 97.1% (83.1% rms) or 30.9 dB (15.4 dB rms). It was found experimentally that this controller actually reduced the state cost by 96.3% (80.8% rms) or 28.7 dB (14.3 dB rms). Similar results were found for the G/E test article.[3]

The cost curves showed that reducing the order of the compensator had essentially no effect on controller performance, and the compensators designed using optimal projection performed no better that those derived from the design model and then reduced. Additionally, it was observed that increasing the order (above 14 states) of the compensators implemented had no effect on closed-loop performance. Therefore, all experimental instabilities were attributed to model errors, predicted by the new stability robustness guideline, rather than model or compensator order reduction.

Conclusions

A dynamic modeling capability for plate-like structures with integrated strain actuators was developed using the Rayleigh–Ritz assumed-mode method. It was found that by carefully selecting the assumed modes and incorporating experimentally measured damping estimates, a model of sufficient fidelity for designing high-authority compensators could be obtained.

A control-law development procedure was established that utilized performance measurements and LQG design variables in a consistent manner to design high-authority multivariable compensators. A model order-reduction procedure also was developed to implement the controllers on a real-time digital computer. Further, a stability robustness guideline was determined that aided in predicting, a priori, the amount of control authority that could be applied to the system without destabilizing high-frequency modes.

Closed-loop benchtop experiments validated the modeling and control-law development procedures, and demonstrated the ability of integrated strain actuators to effect high-authority multivariable control on flexible plate-like structures. The results showed that considerable disturbance attenuation could be achieved throughout large bandwidths containing several flexible modes. The controllers implemented reduced the quasisteady response by over 10 dB and the response of the first flexible mode by over 30 dB. These high-performance controllers decreased the rms response of the system by more than 83%.

Acknowledgments

This work was supported by the General Dynamics Corporation with Mike Love and Jon Bohlmann serving as Technical Monitors.

References

[1]Lazarus, K. B., and Crawley, E. F., "Induced Strain Actuation of Composite Plates," Massachusetts Inst. of Technology, GTL Rept. 197, hbox-Cambridge, MA, 1989.

[2]Lin, C. Y., Crawley, E. F., and Heeg, J., "Open and Closed Loop Results of a Strain Actuated Active Aeroelastic Wing," *Journal of Aircraft* (to be published).

[3]Lazarus, K. B., "High-Authority Multivariable Control of Strain Actuated Plate-Like Active Lifting Surfaces," Ph.D. Thesis, Dept. of Aeronautics and Astronautics, Massachusetts Inst. of Technology, Cambridge, MA, 1992.

[4]Lee, C.-K., and Moon, F. C., "Laminated Piezopolymer Plates for Torsion and Bending Sensors and Actuators," *Journal of the Acoustical Society of America*, Vol. 85, No. 6, 1989.

[5]Wang, B.-T., and Rogers, C. A., "Laminated Plate Theory for Spatially Distributed Induced Strain Actuators," *Journal of Composite Materials*, Vol. 25, No. 4, 1991, pp. 433–452.

[6]Meirovitch, L., *Analytical Methods in Vibrations*, Macmillan, New York, 1967.

[7]Meirovitch, L., and Kwak, M. K., "Convergence of the Classical Rayleigh–Ritz Method and the Finite Element Method," *AIAA Journal*, Vol. 28, No. 8, 1990, pp. 1509–1516.

[8]Blevins, R. D., *Formulas for Natural Frequency and Mode Shape*, Krieger, Malabar, FL, 1984.

[9]Crawley, E. F., and Dugundji, J., "Frequency Determination and Non-Dimensionalization for Composite Cantilever Plates," *Journal of Sound and Vibration*, Vol. 72, No. 1, 1980, pp. 1–10.

[10]Crawley, E. F., and Lazarus, K. B., "Induced Strain Actuation of Isotropic and Anisotropic Plates," *AIAA Journal*, Vol. 29, No. 6, 1991, pp. 944–951.

[11]Moore, B. C., "Principal Component Analysis in Linear System: Controllability, Observability, and Model Reduction," *IEEE Transactions on Automatic Control*, Vol. AC-26, 1981, pp. 17–31.

[12]Mercadal, M., "Homotopy Approach to Optimal, Linear Quadratic, Fixed Architecture Compensation," *Journal of Guidance, Control, and Dynamics*, Vol. 14, No. 6, 1991, pp. 1224–1233.

[13]Lehtomaki, N. A., Castanon, D. A., Levy, B. C., Stein, G., Sandell, N. R., Jr., and Athens, M., "Robustness and Modeling Error Characterization," *IEEE Transactions on Automatic Control*, Vol. AC-29, No. 3, 1984, pp. 212–220.

[14]Maciejowski, J. M., *Multivariable Feedback Design*, Addison–Wesley, Reading, MA, 1989.